



CHORUS

This is the accepted manuscript made available via CHORUS. The article has been published as:

Turning strategies for plunging elastic plate propulsor

Peter D. Yeh, Ersan Demirer, and Alexander Alexeev

Phys. Rev. Fluids **4**, 064101 — Published 12 June 2019

DOI: [10.1103/PhysRevFluids.4.064101](https://doi.org/10.1103/PhysRevFluids.4.064101)

Turning strategies for plunging elastic plate propulsor

Peter D. Yeh, Ersan Demirer, and Alexander Alexeev*

George W. Woodruff School of Mechanical Engineering, Georgia Institute of Technology

(Dated: May 16, 2019)

Abstract

We use three-dimensional computer simulations to examine turning strategies for a biomimetic oscillating elastic rectangular plate propulsor submerged in a viscous fluid. The elastic plate is actuated near the first natural frequency at the leading edge. Two kinematic actuation patterns are probed to produce both pitching and yaw moments: 1) periodic plunging with asymmetric velocities on the upstroke and downstroke and 2) combined sinusoidal plunging and twisting motion. Both strategies lead to net lateral forces and turning moments. For the first case, we find that the magnitudes of the force and turning moment increase with the degree of asymmetry in the stroke. For the second case, our simulations reveal a range of optimal phase angles and twisting amplitudes that lead to the maximum yaw moment.

* alexander.alexeev@me.gatech.edu

I. INTRODUCTION

Fish use a combination of their multiple fins to achieve gradual turning or to accelerate quickly in a different direction to perform an escape maneuver. Weihs [1] extensively studied fish maneuvers using Lighthill's theory, which he adopted for situations where the center of mass follows a curvilinear path. He split the turning motion into several phases and used forces and moment balances to describe the phenomena taking place while fish turn. Notably fish use drag and asymmetric forces produced by dorsal fins to optimize the turning, which is highly efficient when compared to standard ship turning strategies. Sfakiotakis et al. [2] reviewed several swimming mechanisms used by fish highlighting that the main research efforts focused on reproducing body and caudal fin movements. From different turning strategies, the authors indicated flexible actuators as promising approach for the use in fish mimetics. More recently, Tan [3] demonstrated that using a flexible tail is more advantageous than using a rigid tail for maneuvering with a bias angle.

Motivated by the agile performance of fish, a variety of turning designs have been adapted in robotic fish prototypes. Hu et al. [4] proposed a design with a solid body and three servomotors to actuate a flexible tail in order to reproduce sharp turns. The main limitation of their design compared to actual fish was the rigidity of the robotic fish body. The flexibility of a fish from head to tail is essential for the efficient swimming pattern. In the case of their robotic fish only the tail was able to bend, which still yielded sharp turning, yet far from the efficiency found in biological fish.

This approach was further explored by several research groups [5–7]. Multijointed robotic fishes were designed with bodies consisting of segments interconnected by flexible joints. These fishes were able to reproduce sharp turns, however the turning performance was significantly weaker than that found in nature. Moreover, the results showed that the caudal fin plays a critical part in the design enabling sharp turns. A fully biomimetic approach for designing maneuverable robotic fish would require including individually controllable fins. Such a strategy, however, adds another level of complexity to the robotic fish design in terms of implementation, cost, and space requirements. Cen [8] demonstrated that smart materials can be used to create fins with asymmetric beating pattern enabling robotic fish turning, which is a promising scenario integrating maneuvering capabilities into robotic fish using a single fin.

In this study, we use numerical simulations to examine potential turning strategies for

a plunging flexible plate propulsor and quantify the turning performance as a function of actuation parameters. Two turning strategies are considered: 1) asymmetric passive plunging, which leads to a pitching moment and changes the swimming direction in the xz -plane (see coordinate system in Figure 1), and 2) a combination of plunging with rotation, which leads to a yaw moment and changes the swimming direction in the xy -plane. To realize the first strategy, we introduce asymmetry in the plunging pattern by performing the upstroke and downstroke with different velocities. We find that the net lift force and pitching moment increase with the ratio between upstroke and downstroke velocities. The use of second strategy produces a lateral force and yaw moment that depend on the phase between plunging and rotation. We find that the lateral force and moment are maximized at a specific range of phase values.

II. COMPUTATIONAL MODEL

In our computational study we consider an oscillating elastic plate fully submerged in a viscous fluid. The oscillating rectangular plate has length L , thickness b , and width w yielding an aspect ratio $\mathcal{A}_R = L/w$. The plate is actuated at the leading edge with different periodic plunging patterns of constant vertical amplitude $A_0 = 0.1L$ (see Figure 1) and constant frequency ω . The plate is submerged within an incompressible Newtonian fluid with viscosity μ and density ρ , leading to a constant Reynolds number $Re = \rho\omega A_0 L/\mu = 250$.

The plate deformation is dictated by the ratio of the actuation frequency to the natural frequency of the plate. The natural frequency, in turn, depends on the plate mechanical properties, geometry, and mass. In vacuum, the classic beam theory gives the first natural frequency as $\omega_{\text{vac},1} = \frac{\lambda_1^2}{L^2} \sqrt{\frac{EI}{\rho_s b w}}$, with $\lambda_1 = 1.875$ being the first positive root of $1 + \cosh \lambda_n \cos \lambda_n = 0$. Here, ρ_s is the density of the solid plate and EI is the bending rigidity. In a viscous fluid, this natural frequency is shifted due to the added mass effect characterized by the fluid/solid mass ratio $\chi = \rho w/\rho_s b$ and viscous dissipation [9]. The linear theory estimates the first natural frequency in a fluid $\omega_{f,1}$ for high aspect ratio, isotropic plates as $\omega_{f,1} = \frac{\lambda_1^2}{L^2} \sqrt{\frac{EI}{\rho_s b w}} [1 + \frac{\pi}{4} \chi \Gamma(\omega_{f,1})]$ with Γ being the hydrodynamic function that depends recursively on $\omega_{f,1}$ [9]. In this study, we consider resonance oscillations of the plate leading to larger plate deflections and maximizing the propulsion [10, 11]. We, therefore, set the bending rigidity of the plate EI such that the actuation frequency ω in our simulations is equal to the plate natural frequency $\omega_{f,1}$.

When a plate plunges in the vertical direction sinusoidally, the drag force on the upstroke cancels with the drag force on the downstroke. In order to create a net force normal to the plate (for flows with a finite Reynolds number), the actuation pattern must be asymmetric between the upstroke and the downstroke. Because the drag forces during the strokes is a function of velocity normal to plate, a simple mechanism to create a net drag is to actuate the upstroke and downstroke at different velocities.

Following this principle for the first turning strategy, we actuate the leading edge with the following asymmetric plunging pattern:

$$A(t) = \begin{cases} A_0 \cos[\pi/\tau_1(t - n\tau)] & n\tau \leq t \leq n\tau + \tau_1 \\ -A_0 \cos[\pi/\tau_2(t - \tau_1 - n\tau)] & n\tau + \tau_1 \leq t \leq (n + 1)\tau \end{cases} \quad (1)$$

This parametric equation represents motion in two parts. The downstroke motion is a half-cosine wave with amplitude A_0 and half-period τ_1 . The upstroke motion is also a half-cosine wave with the same amplitude, but a different half-period τ_2 . The total stroke period is $\tau = \tau_1 + \tau_2 = 2\pi/\omega$, and n is the current period number. The maximum speed on the downstroke is $v_1 = A_0\pi/\tau_1$ and upstroke is $v_2 = A_0\pi/\tau_2$. We consider values of velocity ratios, v_1/v_2 ranging from 1 to 14, so that the downstroke is faster than the upstroke. This particular actuation pattern is suitable because the motion has continuity in both displacement and velocity. Figure 1c illustrates the asymmetric plunging stroke during one period for different values of velocity ratio.

We expect that the asymmetric plunging pattern on the leading edge would result in an asymmetric plunging response on the remainder of the flexible plate, thereby creating a net force in the direction of plunging. The plate is actuated such that the total stroke period τ corresponds to the first natural frequency in fluid, and the deformation response would be amplified near the trailing edge. In this way the net hydrodynamic force is acting at a location off-center and closer to the trailing edge, which creates the necessary pitching moment in order to change direction within the xz -plane.

Our second strategy to create a turning motion is to combine sinusoidal plunging with a sinusoidal rotation. This actuation pattern is similar to simplified models of insect hovering flight [12], although in this case the application is for generating a net lateral force perpendicular to the swimming direction in the xy -plane. We apply this combined plunging-rotation actuation pattern on the leading edge of the passive flexible swimmer. As shown in Figure 1b, the center of the leading edge is prescribed with sinusoidal plunging $A(t) = A_0 \cos(\omega t)$, where A_0 is the plunging amplitude. The leading edge also undergoes a sinusoidal rotation

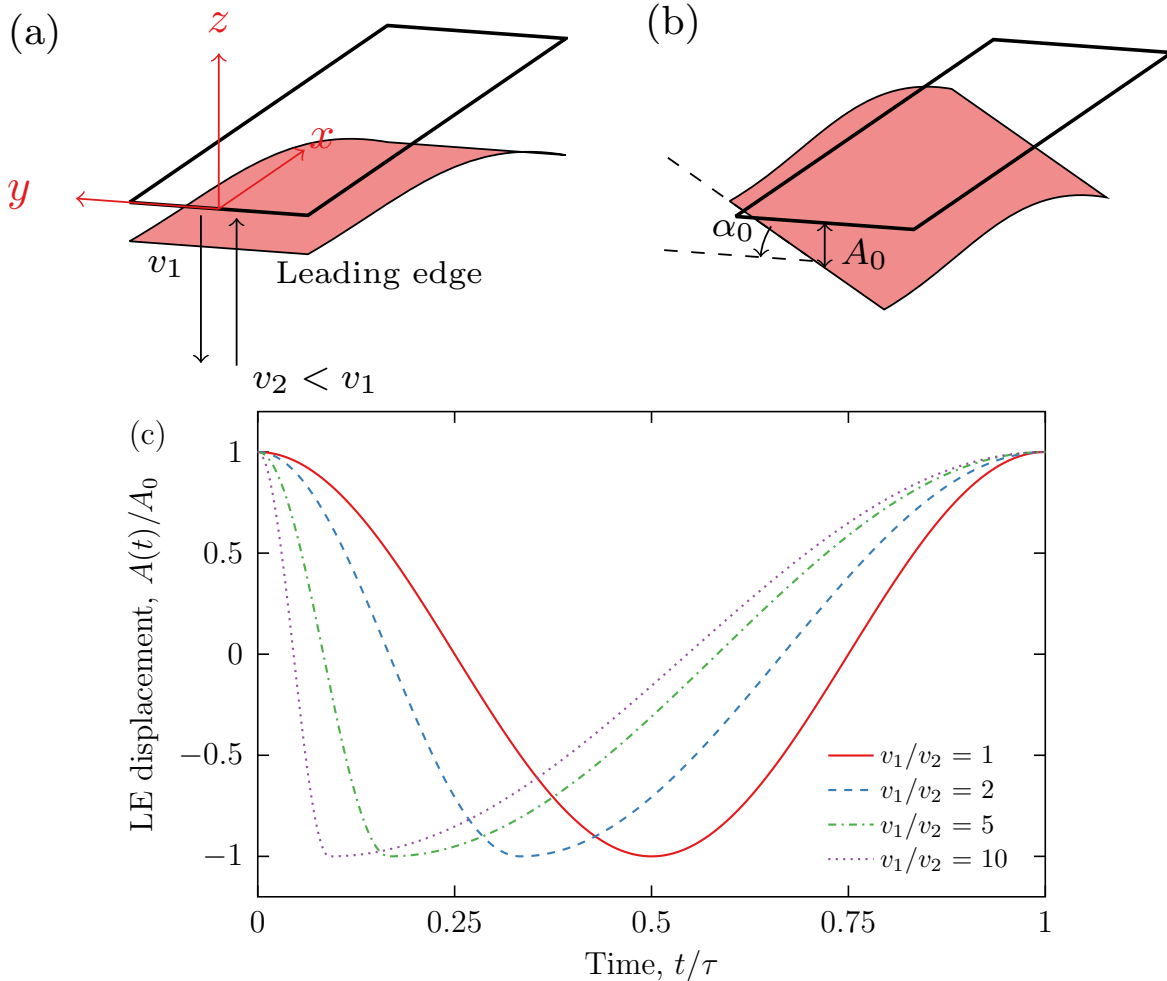


FIG. 1: Schematics of (a) asymmetric plunging actuation and (b) combined plunging and rotation as turning strategies for biomimetic flexible plate swimmer. The black outline indicates the zero-displacement plate position. (c) Plots of the leading edge displacement for different values of velocity ratio v_1/v_2 as asymmetric plunging strategy.

with a tunable phase, given by $\alpha(t) = \alpha_0 \cos(\omega t + \psi)$, where α_0 is the rotation amplitude and ψ represents the phase difference between rotation and plunging.

We expect that the resulting kinematics and deformation response of the plate would lead to a motion that is asymmetric in the y -direction, thus creating a net lateral force and yawing moment. The lateral force and turning moment is expected to be a function of the phase ψ and rotational amplitude α_0 . We set the actuation frequency to the swimmer's first natural frequency and measure the forces and moments as functions of ψ and α_0 .

A three-dimensional fully-coupled fluid-structure interaction solver is used to compute the combined fluid flow and elastic plate response. Our hybrid lattice Boltzmann (LBM)

and lattice spring model (LSM) has been used and validated previously [13–18] including plate propulsor studies [10, 11, 19–21]. Briefly, LBM [22–24] is a particle-based method for simulating fluid flow. In LSM [25, 26], the continuous plate is discretized into a network of masses connected by springs. The models are coupled through boundary conditions [13], where the LSM solid surface acts as a no-slip and no-penetration boundary for fluid represented by LBM [27], while hydrodynamic forces computed from LBM are acted upon the LSM solid [13].

The LSM uses a triangular lattice of mass nodes to represent the elastic plate. The lattice spacing is about 1.4 LBM units. The plate is located at the center of the fluid computational domain, which has size $8L \times 6L \times 8L$, where $L = 50$ is the length of the plate. Here and in what follows all dimensionless values are given in LBM units. We use a refined LBM grid of size $4L \times 3L \times 3L$ around the oscillating plate in order to accurately resolve the flow near the plate surface. The fine grid is coupled at the boundaries to the coarse grid filling the rest of the domain [28]. The grid spacings are $\Delta_{f,r} = 1$ and $\Delta_{f,c} = 2$ for the refined and coarse grid, respectively. The far field boundaries of the coarse grid have impenetrable wall boundary conditions and are located sufficiently far to not impact the flow near the oscillating plate. We use an oscillation period $\tau = 2\pi/\omega = 2000$, the plunging amplitude of $A_0 = 0.1L$, and set the fluid density $\rho = 1$ and the fluid viscosity to yield $Re = 250$. Furthermore, we examine plates with aspect ratios \mathcal{A}_R equal to 1 and 2.5, and fluid/solid mass ratios χ equal to 1, and 2. Details of the implementation of our computational model can be found elsewhere [29].

We define the following scales to non-dimensionalize our quantities of interest: characteristic length is the length of the plate L , characteristic time is the oscillation period τ , characteristic velocity is $U_0 = \omega A_0$, characteristic force is $F_0 = \frac{1}{2}\rho U_0^2 w L$, characteristic power is $P_0 = \frac{1}{2}\rho U_0^3 w L$, and characteristic moment in the z -direction is $M_{z0} = 2I_{zz}^m/\tau^2$, where $I_{zz}^m = \frac{m}{12}(L^2 + w^2)$ is the z -axis mass moment of inertia. The later definition of the characteristic moment approximates the pitch angle change per stroke period in the absence of fluid resistance.

III. RESULTS AND DISCUSSION

We first assess the turning performance of asymmetric plunging swimmers with velocity ratios ranging from 1 to 14. Typical flow structures generated by such swimmers are

illustrated in Video S1 in the Supplementary Information [30]. In Figure 2, we plot the period-averaged net thrust (x -direction), and lift force (z -direction), as a function of the velocity ratio for several values of fluid/solid and aspect ratios.

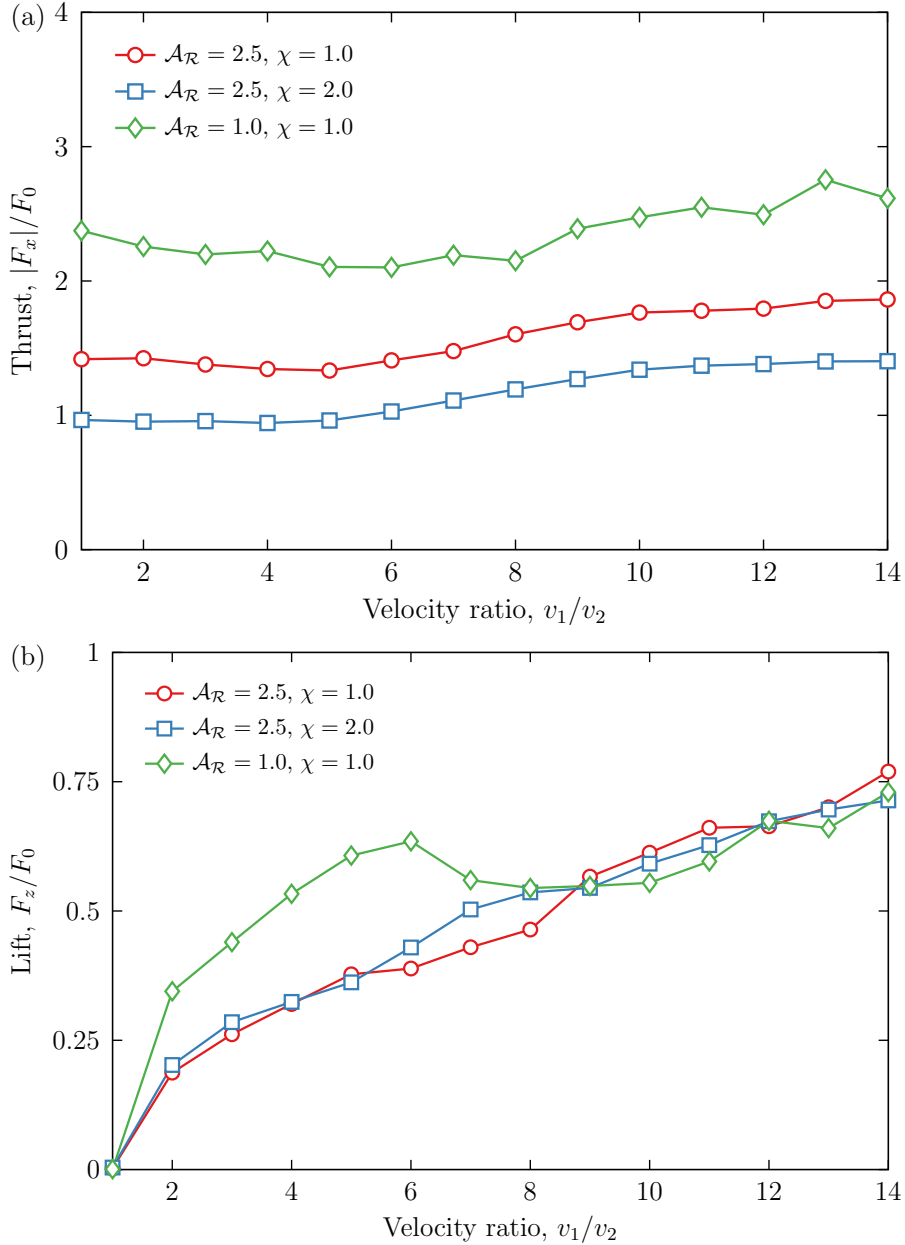


FIG. 2: (a) Lift force and (b) thrust force generated by asymmetric plunging swimmer as a function of the velocity ratio.

We find that the thrust generated by plunging swimmers only slightly changes as a function of the velocity ratio with a minor increase with increasing velocity ratio. This behavior is independent of the fluid/solid ratios and aspect ratios we tested. The magnitude of the thrust decreases for heavier and increases for wider swimmers. This is consistent

with previously reported results [10, 11]. The increase in the generated thrust for heavier swimmers is related to the greater bending of such swimmers at resonance leading to larger trailing edge (TE) displacement as shown in Figure 3. Forward thrust is proportional to the TE displacement which is suppressed when the relative mass of displaced fluid increases for lighter swimmers. Note that the magnitude of the TE displacement increases with increasing velocity ratio. This increase is due to faster accelerations experienced by the plunging elastic swimmer as v_1/v_2 increases. The increase of the TE displacement with v_1/v_2 explains the increase in the thrust with v_1/v_2 shown in Figure 2a. The TE displacement and deflection are insensitive to the swimmer aspect ratio (Figure 3a and 3b). Since wider swimmers experience lesser effect of side edge vortices [31], such swimmers can generate greater thrust for the same actuation pattern.

Whereas increasing velocity ratio has only a minor effect on the thrust generation, it does strongly affect the lift force generated by the asymmetrically plunging elastic swimmer (Figure 2b). We find that the lift force increases with increasing v_1/v_2 . The higher the velocity ratio, the larger the asymmetry exists between the upstroke and downstroke, leading to a larger net lift force. Remarkable that the magnitude of the lift force is almost independent of the mass ratio. Furthermore, the wider swimmer with $\mathcal{A}_R = 1$ slightly outperforms the narrow swimmer with $\mathcal{A}_R = 2.5$ for $v_1/v_2 < 8$. This indicates that the magnitude of the TE displacement alone is not a significant factor in the production of the lift force.

To further examine the generation of lift force by asymmetric plunging, we characterize the asymmetry of the resulting bending pattern. We use the difference between the drag forces experienced by the plate between up and down strokes to quantify the stroke asymmetry. Since the drag force is proportional to the velocity squared, we evaluate the root mean square velocities U_{rms} of the upstroke and downstroke at the plate trailing edge. In Figure 3b we plot ΔU_{rms} , which represents as the difference between the root mean square velocities of the upstroke and downstroke as a function of the velocity ratio. We find that the asymmetry of U_{rms} increases with an increasing velocity ratio up to v_1/v_2 about 10, after which it either saturates or decreases. This explains a weak sensitivity of lift force in Figure 2b to the values of added mass and plate aspect ratio. We further note that the bending pattern of the wide plate exhibits more complex motion than the narrow plates including a range of higher frequency oscillation modes. These oscillation modes are excited due to the discontinuity of the higher derivatives of the actuation pattern given by Eq 1 and are enhanced with increasing v_1/v_2 .

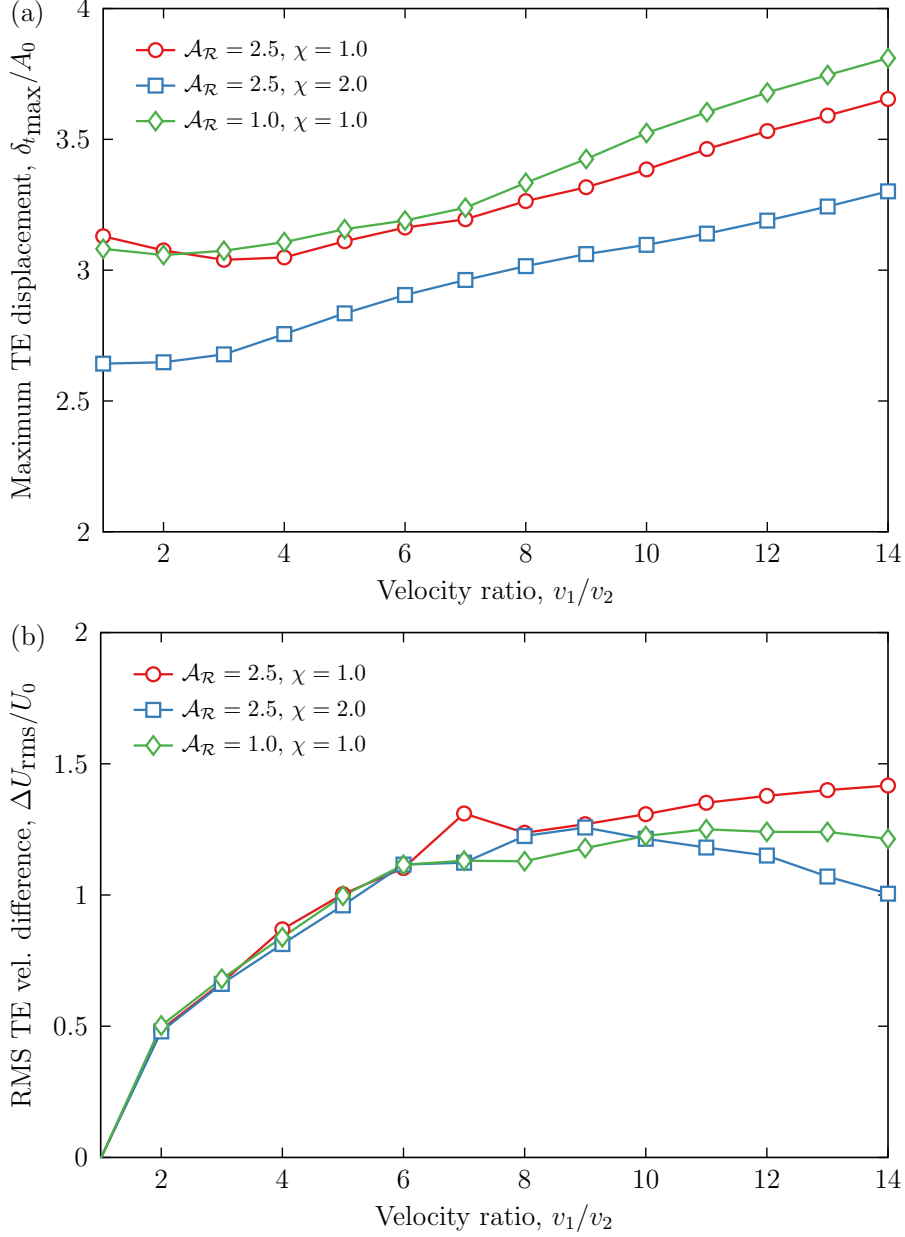


FIG. 3: (a) Maximum trailing edge displacement and (b) difference between root mean square trailing edge upstroke and downstroke velocity as a function of the velocity ratio.

While the lift force can displace the swimmer side-wise, it does not necessarily result in the swimmer changing spatial orientation and, therefore, propulsion direction. To assess the ability of asymmetric plunging to change the swimmer's swimming direction we evaluate the turning moment M_y generated by plunging actuation with different velocity ratios. The turning moment M_y is calculated with respect to the y -axis through the plate's centroid.

We find that the turning moment M_y exhibits a non-monotonic behavior with the velocity ratio. This is in spite of a nearly monotonic increase of the lift force generated by the plate

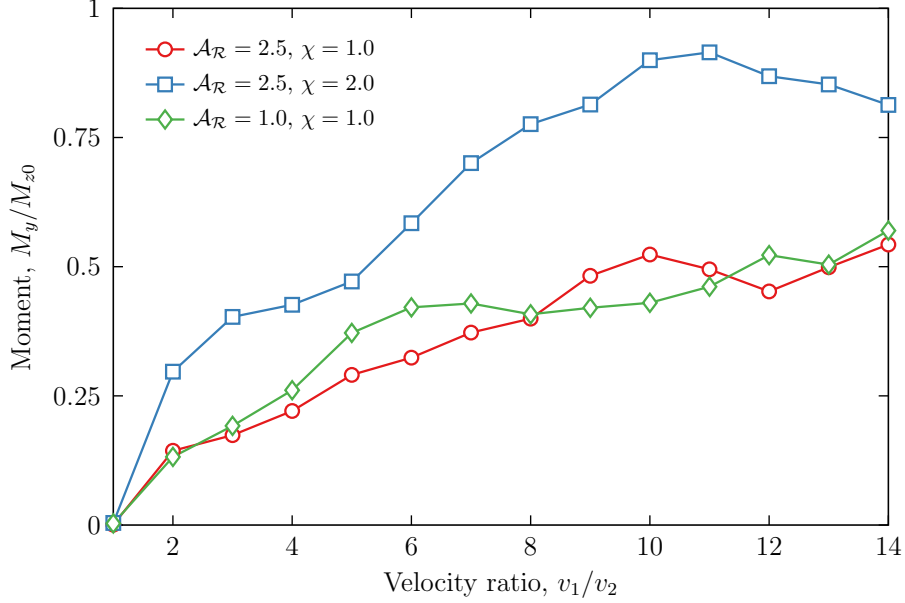


FIG. 4: Turning moment on asymmetric plunging swimmer as a function of the velocity ratio.

for $v_1/v_2 \leq 14$. Interestingly, for the narrow plate the moment increases almost linearly until $v_1/v_2 \simeq 10$, whereas the wider plate exhibits fluctuations of the moment which can be attributed to higher frequency modes emerging during the plate oscillations. Although the lift is not a strong function of the fluid/solid ratio, the pitching moment depends strongly on this ratio. The moment increases roughly linearly with the fluid/solid ratio for the heavier plate. This result suggests that the changing mass ratio shifted the point of application of the lift force, magnitude of which in turn remains insensitive to the mass ratio.

To quantify the turning efficiency, we define two efficiency parameters $\varepsilon_{Fx} = \frac{F_x/F_0}{P_{\text{input}}/P_0}$ and $\varepsilon_{My} = \frac{M_y/M_{z0}}{P_{\text{input}}/P_0}$ that represent respectively the thrust and the moment efficiency. Their values are plotted in Figure 5a. We find that the thrust efficiency decreases with an increasing velocity ratio indicating an increased losses due to formation of side edge vortices. The thrust efficiency is nearly independent of the fluid/solid ratio, yet it depends on the plate aspect ratio. The later can be explained by a reduced relative contribution of side vortices to the efficiency of the wider swimmer. The moment efficiency shown in Figure 5b exhibits an opposing trend. Here, the efficiency strongly depends on the fluid/solid ratio and remains independent of the plate aspect ratio. The efficiency is maximized for lower velocity ratios after which it gradually decreases that can be attributed to increasing viscous losses and therefore increasing input power. For the two lightest swimmers the maximum

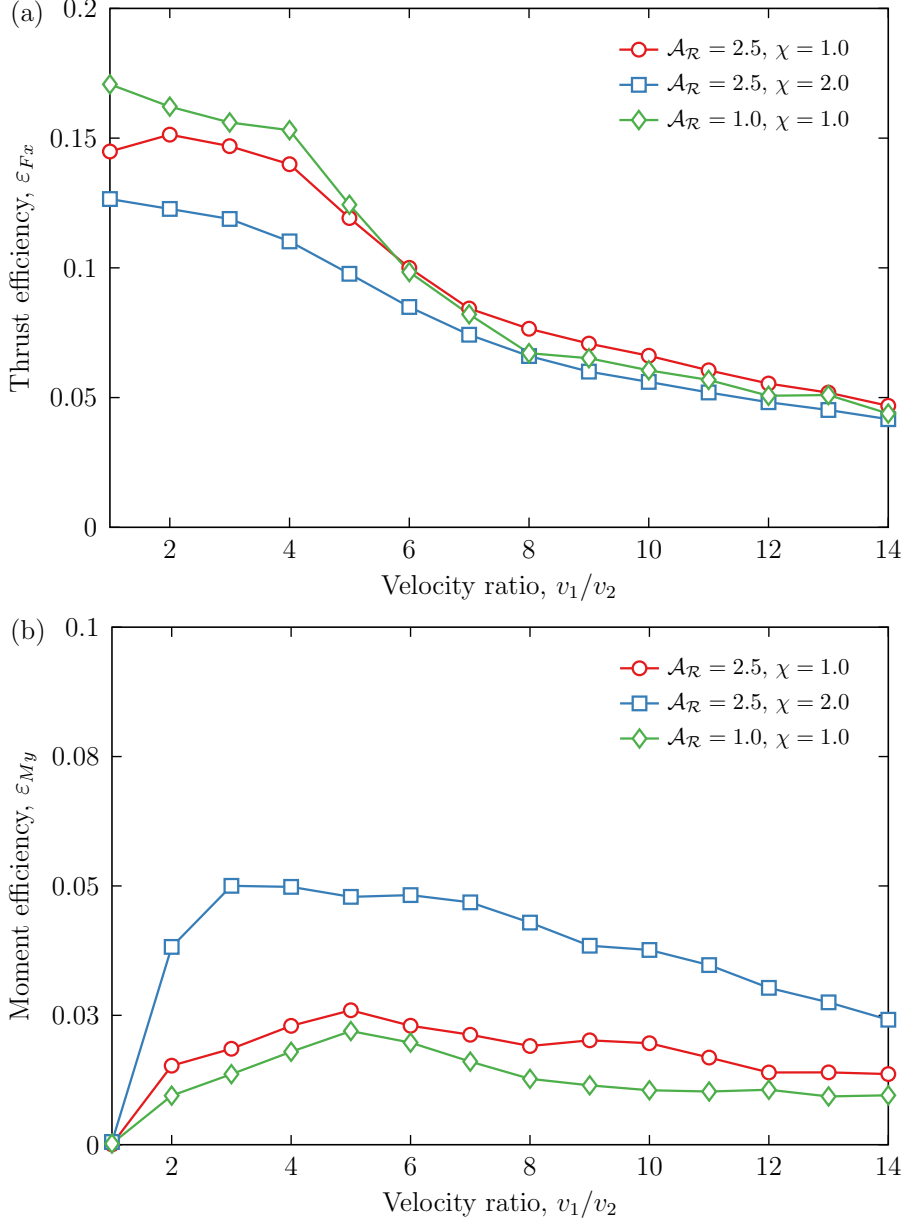


FIG. 5: (a) Thrust and (b) pitching moment efficiency on asymmetric plunging swimmer as a function of the velocity ratio.

moment efficiency takes place for $v_1/v_2 = 3$. Thus, for the efficiency point of view the plate should be operated with relatively small velocity ratios in the range below approximately 5. Using higher velocity ratios leads to sub-optimal performance that can be attributed to the contribution of the higher oscillation modes.

To provide a further insight into the turning moment behavior, we examine $v_1/v_2 = 5$ as a representative case and plot in Figure 6a the time history of the leading and trailing edge displacements for one period. We find that the trailing edge motion represents as a

combination of the stroke frequency (remember the swimmer period corresponds to the plate natural frequency in fluid) and higher frequency oscillations. A closer examination shows that one of the more pronounced higher frequencies is the frequency of the downstroke.

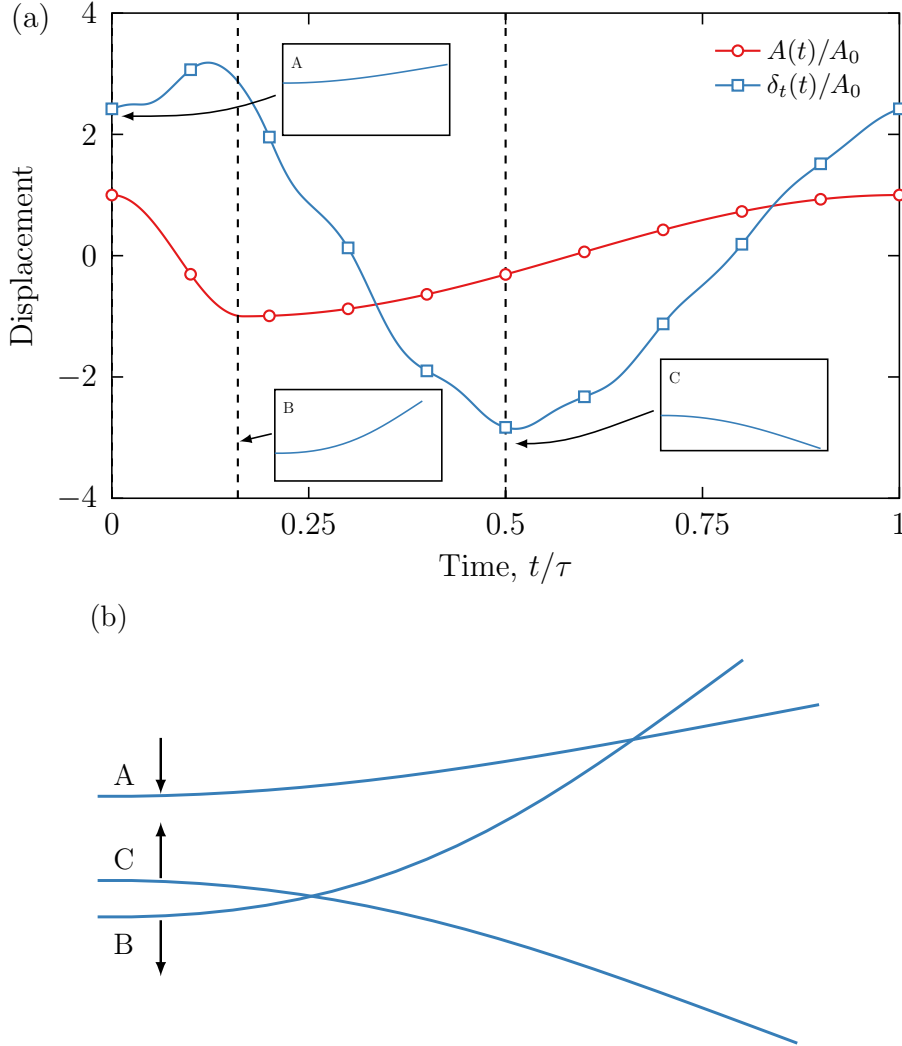


FIG. 6: (a) Displacement time history with (b) bending profile at times A, B, and C, corresponding to times $t/\tau = 0, 0.16$, and 0.5 , respectively. The asymmetry in the bending pattern is mainly caused by the quick movement from A to B.

The higher frequency oscillations of the trailing edge imply that the hydrodynamic force experienced by the plate also exhibits the higher frequency oscillations. This multimodal excitation can be used to explain the non-monotonic behavior of the turning moment at higher velocity ratios. Thus, we conclude that the velocity ratio allows us to directly control the pitching moment for sufficiently small velocity ratio values, below ~ 10 in our system.

Snapshots of the bending pattern are plotted in Figure 6b at the representative times as

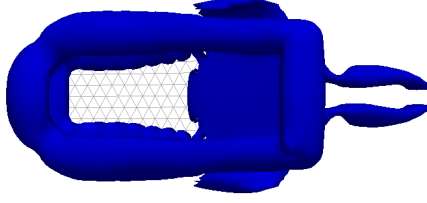
indicated on Figure 6a with the vertical dashed lines. Point A ($t/\tau = 0$), shows the bending pattern of the plate at the start of the downstroke just before the swimmer accelerates downward. At this time, the trailing edge is located at approximately 80% of its peak amplitude. At point B ($t/\tau=0.16$), the plate has finished the downstroke. Because of the high velocity, the trailing edge does not have time to respond and still stays near its peak amplitude. Near point B, the relative deflection is maximized. After that the leading edge slowly moves upwards, whereas the trailing edge continues to move downwards dominated by the plate’s natural frequency. At point C ($t/\tau = 0.5$), the trailing edge is located at its minimum position, after which it begins its upstroke until it reaches the position at the beginning of a period. From these bending patterns we observe that the trailing edge response is relatively symmetric about the equilibrium position, but the motion of the leading edge imposes the asymmetry in the kinematics, particularly through the motion between the points A and B.

The vorticity contours plotted in Figure 7 for, respectively, a narrow swimmer and a wider swimmer provide further insights in the understanding of the swimmer performance. Both swimmers display similar flow structures composed of trailing edge vortices (TEV) and side edge vortices (SEV). The combination of SEV and TEV detaching from the trailing edge form a horseshoe structure in the wake of the swimmer. Side edge vortices create vortex-induced drag, which has preponderant contribution to overall drag experienced by the oscillating elastic swimmers. We find that the characteristic sizes of SEV are similar for both swimmers. As a result, the wider swimmer produces a lower overall drag per width compared to the more narrow swimmer, which explains the enhanced thrust performance of the wider swimmer shown in Figure 2a.

To evaluate the turning performance of the combined plunging and rotation actuation, we simulate a plate actuated at the first natural frequency and compute the net forces and moments during a stroke period. Video S2 in the Supplementary Information [30] shows flow structures produced by an elastic swimmer with combined plunging and rotation. In Figures 8a and 8b, we plot the propulsive and lateral forces as a function of phase, ψ . The different lines represent the different values of rotational amplitude, α_0 . Note that the values of $\psi > \pi$ lead to redundant results because $F_x(\psi) = F_x(\psi - \pi)$ and $F_y(\psi) = -F_y(\psi - \pi)$ from the symmetry of the problem.

We find that the propulsion decreases with increasing α_0 , but it does not depend strongly on the phase ψ . This is due to the fact that the projected area in the plunging direction

(a)



(b)

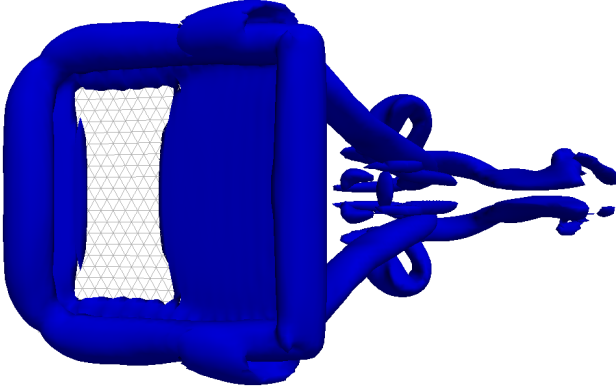


FIG. 7: Surface of constant vorticity magnitude ($\omega = 20$ normalized by leading edge frequency) plotted for $\chi = 1.0$, (a) $\mathcal{A}_R = 2.5$ and (b) $\mathcal{A}_R = 1.0$ at time $t/\tau = 0.16$ which corresponds to point B of figure 6 (top view).

decreases with increasing α_0 . When the swimmer moves vertically, it also rotates, decreasing the projected area. As a result, less fluid is deflected backwards so the resulting thrust is weaker. The thrust curves also imply that the net propulsion can be tuned by increasing or decreasing the rotational amplitude.

In contrast, the lateral force is a strong function of both α_0 and ψ . When comparing at the maximum lateral force for each value of α_0 , we observe that the optimal rotational amplitude is $\alpha_0 = \pi/4$. For this rotational amplitude, we find that the optimal phase to generate the largest lateral force is $\psi = \pi/6$, but this optimum is shallow. When considering the “high-performing” amplitude values of $\pi/6$, $\pi/4$, and $\pi/3$, high lateral force is found in the range between $\psi = -\pi/12$ and $\psi = 5\pi/12$. Similarly, there is also a region between $\psi = 7\pi/12$ and $\psi = 3\pi/4$ that leads to weak lateral force.

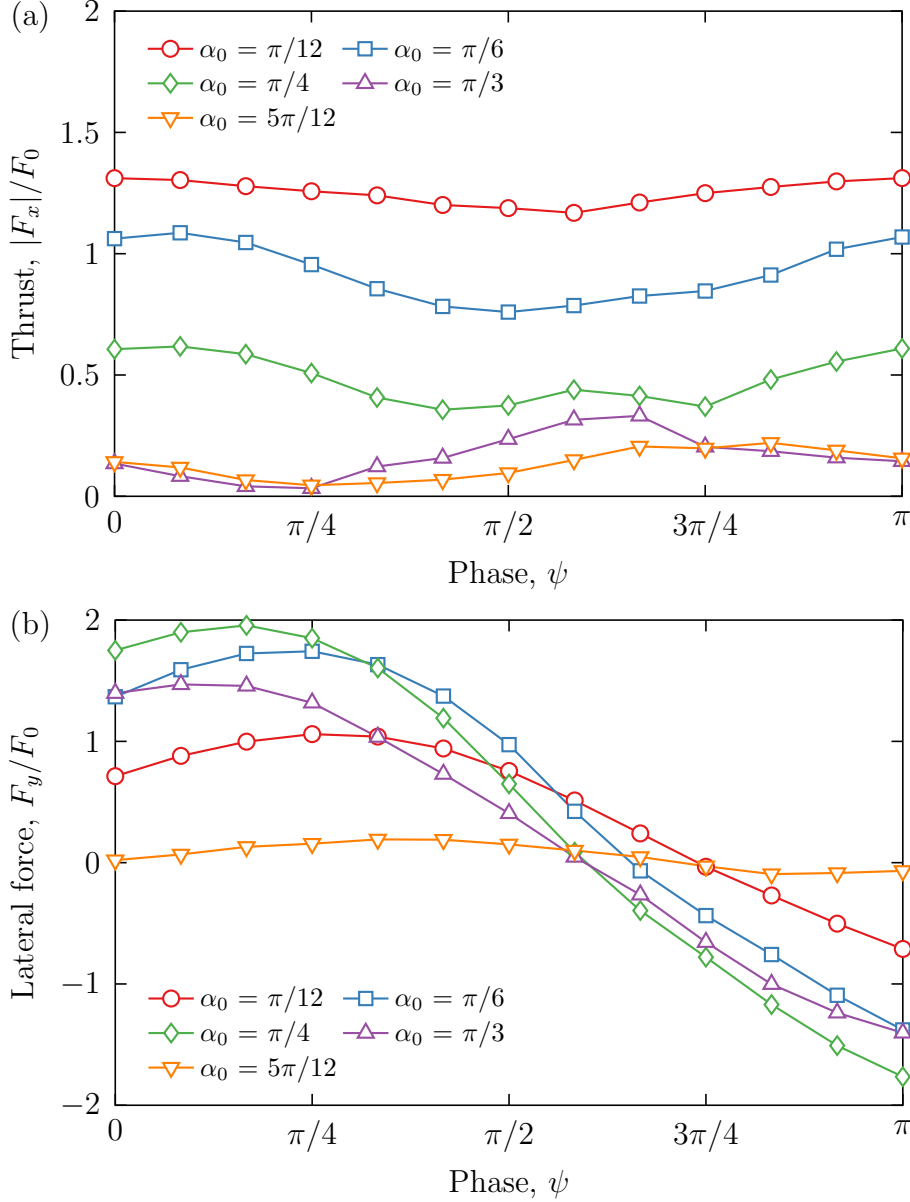


FIG. 8: (a) Propulsive and (b) lateral forces for combined plunging and rotating swimmer.

Propulsive forces decrease with increasing α_0 , which is related to the smaller projected areas for increasing α_0 . Lateral force is maximized in a range of phase values $\psi = -\pi/12$ and $\psi = 5\pi/12$.

A net lateral force itself does not necessarily result in a change in direction. To examine this capability, we compute the net moment due to the fluid, M_z , about the z -axis through the plate's centroid at equilibrium position. The net moment leads to a change in the yaw angle about the z -axis. In Figure 9, we plot the moment as a function of ψ and α_0 . The trends for moment correlate with the trends for the lateral force, suggesting that the net

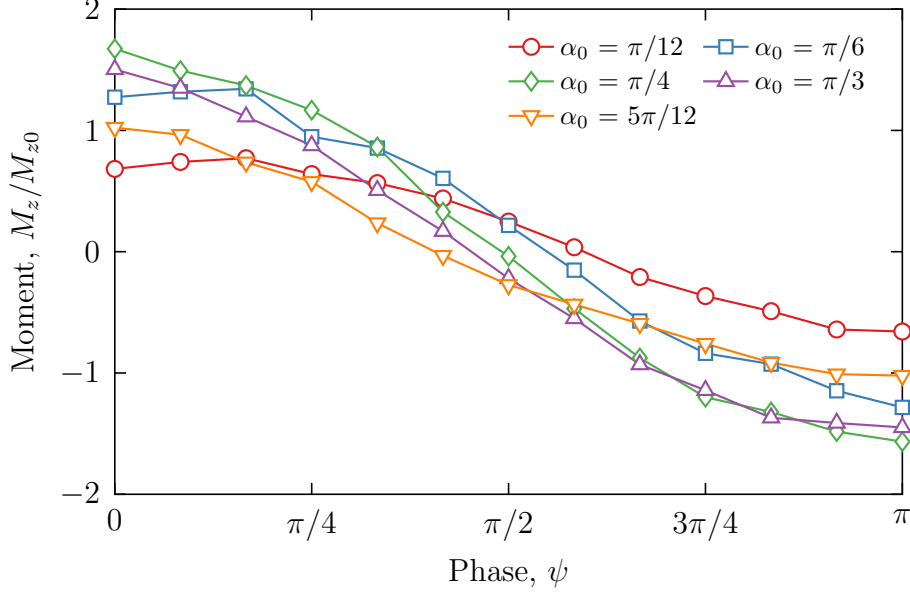


FIG. 9: Turning moment for combined plunging and rotating swimmer. The moment follows similar trends to lateral force.

lateral force is indeed responsible for the yawing moment. Interestingly, we find that for $\alpha_0 = 5\pi/12$, the lateral force is small, but the moment is non-zero. This suggests that a net lateral couple is applied on this particular swimmer, so it can turn without drifting.

Figures 10a and b show the effects of the mass ratio and aspect ratio on the thrust and lateral force for $\alpha_0 = \pi/4$. We find a weak dependency of the thrust on mass ratio, whereas increasing the plate width significantly enhances produced thrust. The larger thrust of wider plate can be associated with more significant plate twisting than that experienced by the narrow plates. This in turn leads to a greater displacement of the trailing edge and, therefore, greater thrust generated by the wider plate.

The lateral force shown in Figure 10b follows a similar trend in terms of its dependence on the mass and aspect ratios, with a high lateral force production range between $\psi = -\pi/12$ and $\psi = \pi/2$. We note that the non-dimensional lateral force magnitude of the wider swimmer is roughly 2.5 times larger than the lateral force magnitude of the narrow swimmer. This suggests that the lateral force scales with the width squared, and therefore the characteristic force experienced by the plate is proportional to the added mass, which scales as Lw^2 .

Figure 11 shows that the turning moment increases with the increasing magnitude of the mass ratio and the aspect ratio. Conversely to the lateral force and thrust, the moment is

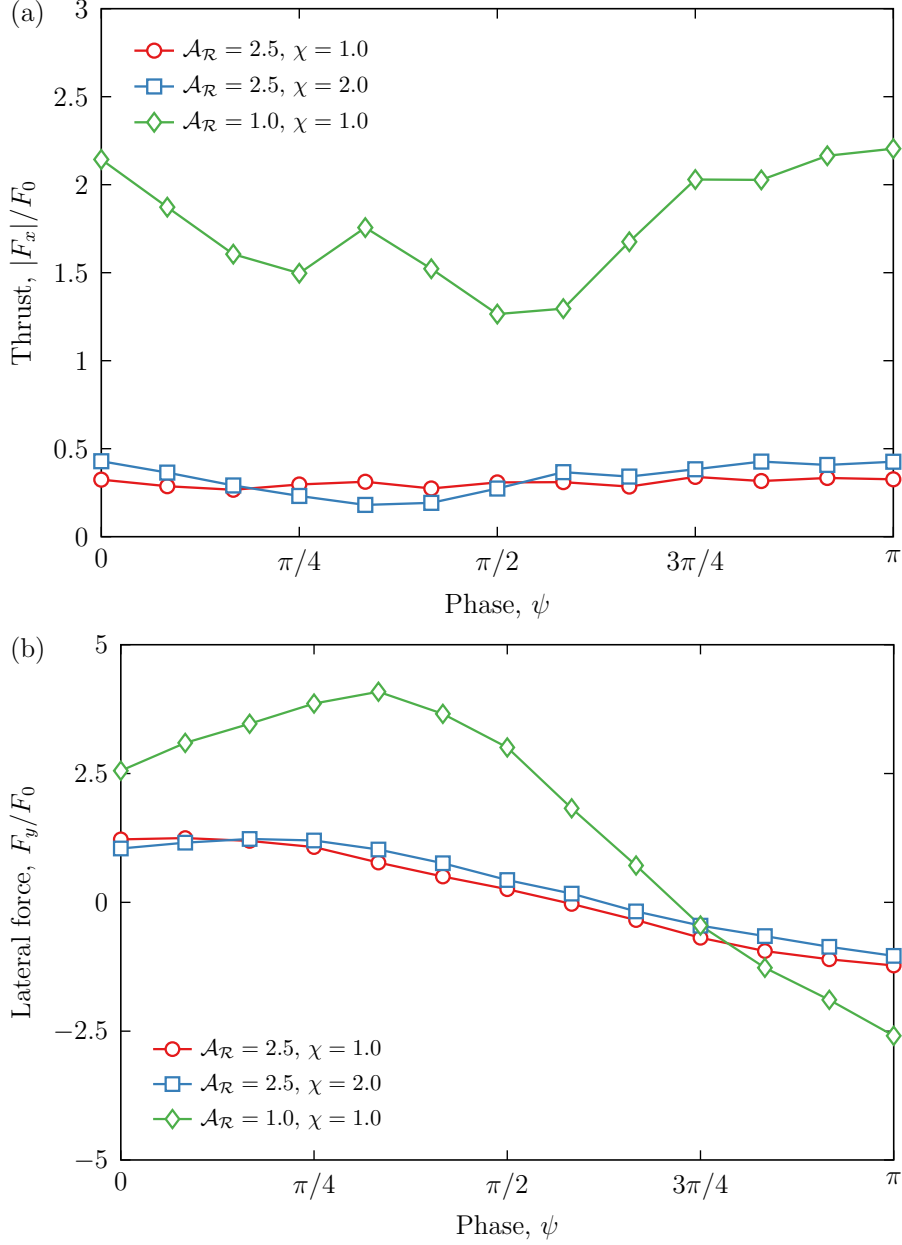


FIG. 10: (a) Propulsive and (b) lateral forces for combined plunging and rotating swimmer for $\alpha_0 = \pi/4$ and several fluid/solid and aspect ratios.

roughly comparable between all the cases. This result indicates that the moment M_{z0} scales with the width squared similar to the magnitude of the lateral force.

In order to understand the mechanism that leads to high lateral force production, we first seek to understand the kinematics of the swimmer response. In Figure 12a, we consider a rotating coordinate system (shown in red), denoted by the $(xyz)'$ axes, that is attached to the leading edge so that the z' -axis is always normal to the leading edge. Figure 12b gives the perspective of the swimmer relative to the $(xyz)'$ axes. We denote the position

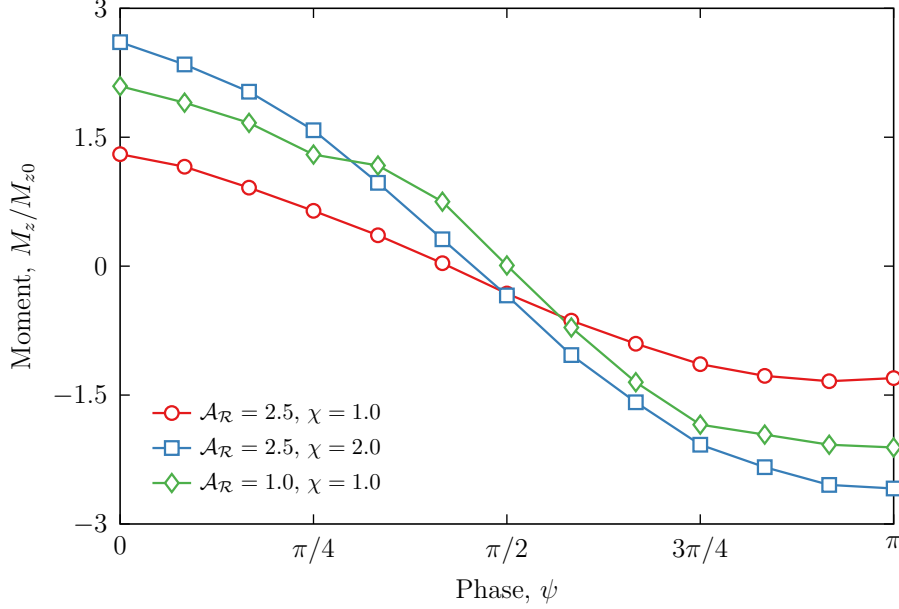


FIG. 11: Turning moment for combined plunging and rotating swimmer for $\alpha_0 = \pi/4$ and several fluid/solid and aspect ratios.

vectors of the maximum extent of the trailing edge corners by \mathbf{r}_{y+} and \mathbf{r}_{y-} . The absolute displacements of the trailing edge corner points are denoted by $\delta_{y,\pm}$ as labeled in Figure 12a. The displacements of these corner points relative to the surface normal are given by $\delta_{\text{rel},y\pm} = \mathbf{r}_{y\pm} \cdot \hat{\mathbf{z}}'$, as labeled in Figure 12b.

In Figure 12c, we plot $\delta_{y\pm}$ and $\delta_{\text{rel},y\pm}$ as functions of ψ for the case $\alpha_0 = \pi/4$. We observe that at low phase angles $\psi < \pi/4$, where lateral force is maximized, the absolute displacements are also maximized, suggesting that the larger displacements yield larger lateral forces. What is interesting though is that the relative displacements of the two trailing edge corner points nearly coincide, showing that the plate undergoes a negligible amount of twisting during the swimming stroke. Therefore, the plate plunges vertically relative to the surface normal, but the surface normal is also continuously changing direction based on $\alpha(t)$.

Another step to understanding the physics behind the lateral force production is to examine the symmetric vertical force production of a plunging plate undergoing no rotation. Figure 13 shows the time histories of the relative trailing edge velocity $v_{TE,r}(t) = \frac{d}{dt}[\delta_t(t) - A(t)]$ and the vertical force. We observe that the maximum (most negative) trailing edge relative velocity has a phase delay of approximately 0.29π to the maximum vertical force, as indicated by the dotted lines. We would expect that the vertical force and velocity are correlated

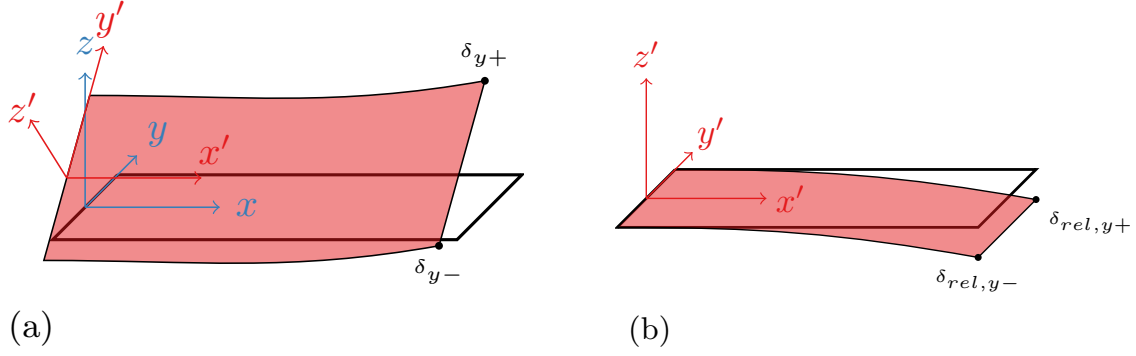


FIG. 12: (a) Schematic showing rotating $(xyz)'$ axes relative to the fixed (xyz) axes. (b) Perspective of swimmer in $(xyz)'$ axes. (c) Absolute and relative deflections of the trailing edge corner points. The relative deflection of the corner points nearly coincide, showing that the swimmer has negligible twist motion.

because the faster a plate moves normal to its surface, the larger drag force it experiences.

Then, we examine the time histories of the rotation angle α , lateral force F_y , moment M_z , and relative trailing edge velocity in the $(xyz)'$ reference frame, $v_{TE,r} = \frac{d}{dt} [0.5(\delta_{rel,y+}(t) + \delta_{rel,y-}(t))]$. The time histories for $\alpha_0 = \pi/4$ and $\psi = \pi/6$, the case which exhibits the largest net lateral force (Figure 8b), are plotted in Figure 14 and provide insight into the lateral force production.

We find first that the maximum moment, lateral force, and rotation angle occur at the same t . Thus, the largest lateral force production occurs at the maximum rotation angle. As Figure 12 suggests, the plate is plunging up and down without twisting, while changing its surface normal. Force production should therefore be primarily normal to the surface. The

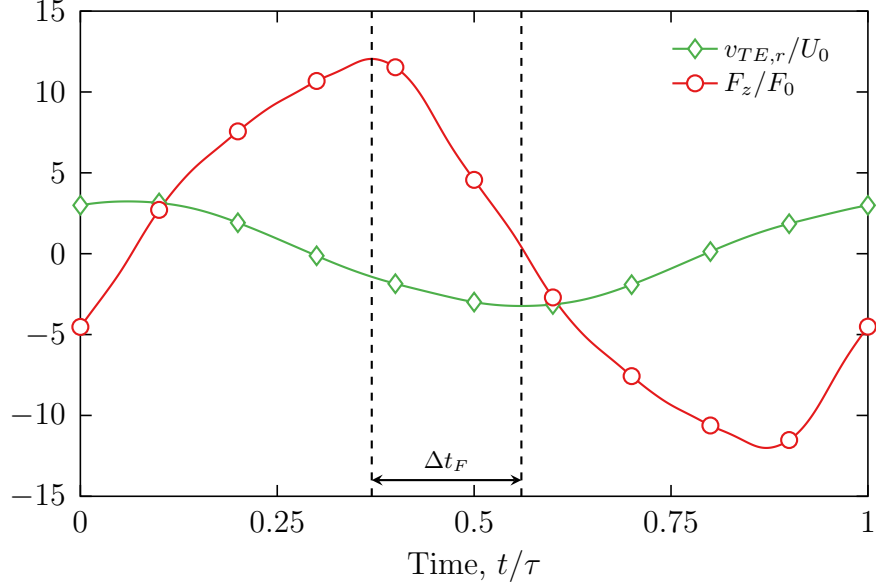


FIG. 13: Time histories of relative trailing edge velocity for a plunging plate with no rotation showing the time of maximum vertical force production relative to the maximum trailing edge velocity.

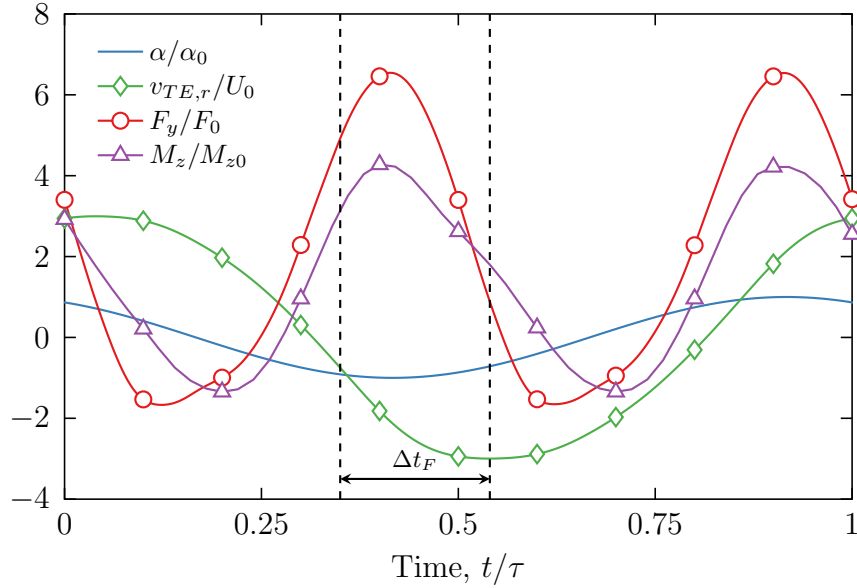


FIG. 14: Time histories for multiple quantities for $\alpha_0 = \pi/4$ and $\psi = \pi/6$. Large lateral force and turning moment are produced because the time of maximum force production based on the relative trailing edge velocity is tuned to the maximum of α .

time history of $v_{TE,r}$ is also shown in Figure 14, where the dotted line represents the time of maximum force production based on the phase difference computed for a plunging swimmer

in Figure 13. The time of the maximum force production coincides closely with the maxima of $\alpha(t)$ and the other quantities. This explains the mechanism of the large lateral force production. The phase difference ψ must be tuned so that the maximum rotation occurs at the same time of maximum force production based on the correlation with $v_{TE,r}$. This way, the largest amount of force produced, which is in the direction normal to the plate surface, can be directed laterally during the stroke.

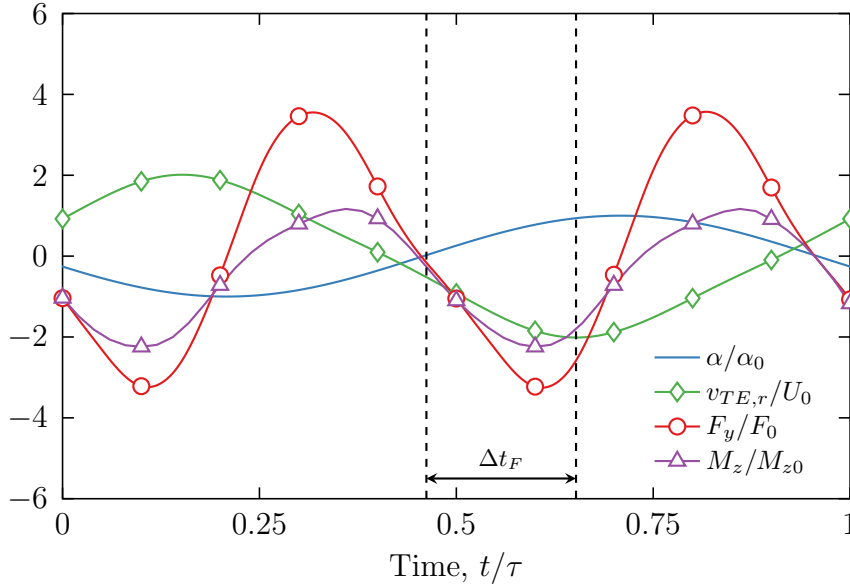


FIG. 15: Time histories for multiple quantities for $\alpha_0 = \pi/4$ and $\psi = 7\pi/12$. Little lateral force and moment production is due to the time of maximum force production occurring when $\alpha \approx 0$, so force is directed vertically, not laterally.

We can also notice that the first peaks of lateral force and moment correspond to a trailing edge downstroke relative to the surface normal based on the negative value of $v_{TE,r}$. At this point, α is negative, which means that in the inertial frame, the downstroke has a $-\hat{y}$ -component, generating a lateral force in $+\hat{y}$ -direction and moment in the $+\hat{z}$ -direction. The second peak corresponds to an upstroke, but now α is positive, so the upstroke has a $-\hat{y}$ -component, generating a force again in the $+\hat{y}$ -direction and a moment again in the $+\hat{z}$ -direction. At the valleys of F_y , the force production is small based on the velocity–relative deflection phase difference and α is small, so force is directed mostly parallel to the \hat{z} -direction. Evidently, tuning ψ to match the force production has also the benefit of reducing unwanted lateral force in the opposite direction.

This principle also explains the poor lateral force and moment production at values of

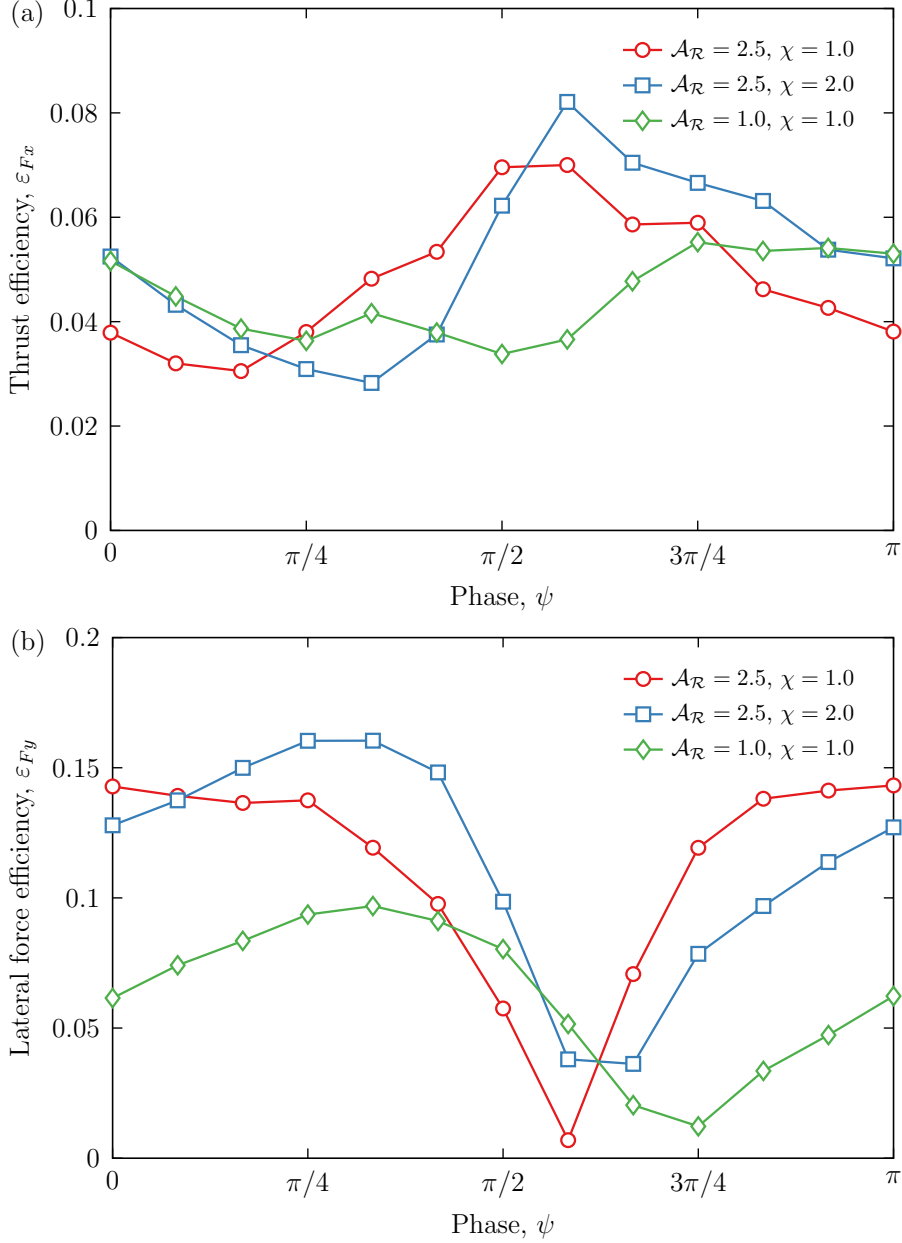


FIG. 16: (a) Propulsive and (b) lateral forces efficiency for combined plunging and rotating swimmer for $\alpha_0 = \pi/4$ and several fluid/solid and aspect ratios.

ψ about $\pi/2$. In Figure 15, we plot the time histories of the same quantities for $\alpha_0 = \pi/4$ and $\psi = 7\pi/12$. We find that the maximum force production is aligned with α when $\alpha \approx 0$, so the maximum force is directed in the $\hat{\mathbf{z}}$ -direction. Furthermore, when α is largest, the time of maximum force production is near zero, and thus the lateral force produced is correspondingly near zero. At the peaks of lateral force and moment, the α value and force production are suboptimal, and the peaks and valleys also cancel each other. Thus, the force production and α are not synchronized, which causes little to no turning moment or

lateral force produced.

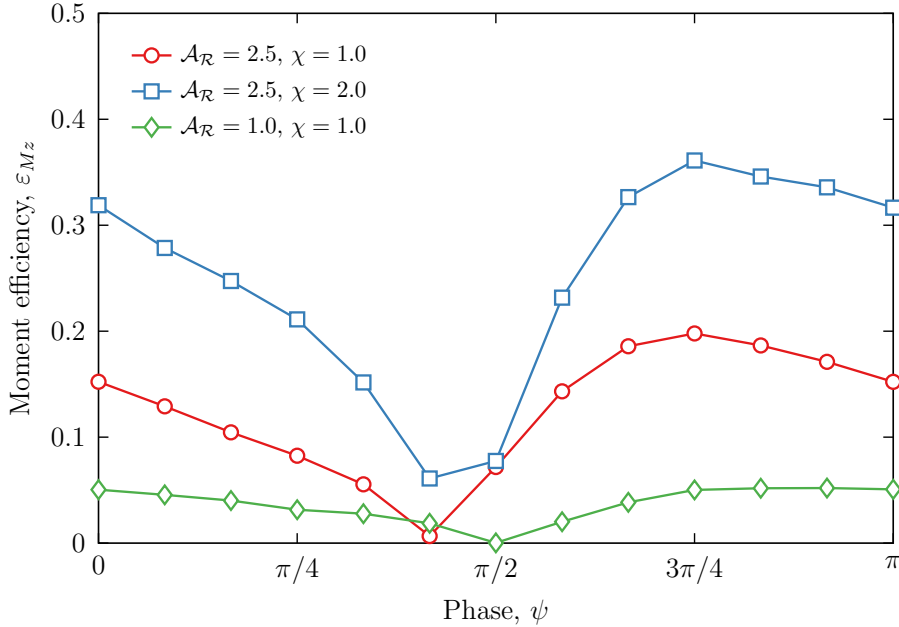


FIG. 17: Turning moment efficiency for combined plunging and rotating swimmer for $\alpha_0 = \pi/4$ and several fluid/solid and aspect ratios.

We quantify the turning performance of combined plunging and rotating motion by defining the following efficiencies $\varepsilon_{Fx} = \frac{F_x/F_0}{P_{\text{input}}/P_0}$, $\varepsilon_{Fy} = \frac{F_y/F_0}{P_{\text{input}}/P_0}$ and $\varepsilon_{Mz} = \frac{M_z/M_{z0}}{P_{\text{input}}/P_0}$ that respectively represent the thrust efficiency, the lateral force efficiency, and the turning moment efficiency. Figure 16a shows that the thrust efficiency is comparable for the three cases considered. Moreover, we find that the maximum of thrust efficiency approximately coincides with the minimum of lateral force efficiency and vice versa. This points to the redistribution of the generated thrust between the forward and lateral directions while keeping the total force about the same. The moment efficiency drops when the maximum force production occurs when $\alpha \simeq 0$ so that the power input mainly feeds the thrust.

The moment efficiency is shown in Figure 17. Its value is minimized for the phase $\psi = \pi/2$ at which the moment is about zero (Figure 11). The maximum of the moment efficiency occurs for $\psi = 3\pi/4$. This phase does not coincide with the phase of the maximum moment, however the moment magnitude at the maximum efficiency is close to the maximum moment magnitude. In contrast to the thrust and lateral force efficiencies, the moment efficiency depends strongly on the mass and aspect ratio. We find that the wider swimmer has the lowest moment efficiency, whereas the lighter swimmer has the strongest moment efficiency. Thus, lighter and more narrow swimmers are beneficial both in terms of turning moment

production and turning moment efficiency.

IV. CONCLUSION

We studied two strategies for steering an oscillating flexible plate swimmer by changing actuation patterns. The first strategy was to impose a plunging motion with a faster velocity on the downstroke compared to the upstroke. This created a pitching moment. We found that the asymmetric plunging stroke created a net lift force on the trailing edge during each stroke period, which contributed to a turning moment. The magnitude of the lift force increased monotonically with increasing velocity ratio, whereas the pitching moment exhibits a maximum around $v_1/v_2 = 10$. The asymmetry of the bending pattern was mainly associated with the trailing edge delay during the fast downstroke.

The second strategy was to combine sinusoidal plunging with sinusoidal rotation, which resulted in a yawing moment. We investigated the lateral force production as a function of the rotation amplitude and phase difference between plunging and rotation. We found a range of optimal phase angles in which lateral force and moment production is best. Furthermore, we examined the resulting plate kinematics and found that the bending is primarily normal to the surface with negligible twisting motion. We examined the time history of relative trailing edge velocity and force production, and showed that in order to optimize turning moment and lateral force, the phase must be tuned so that the instant of time during maximum rotation coincides with the instant during maximum force production.

V. ACKNOWLEDGMENTS

We thank the National Science Foundation (CBET-1705739) for financial support.

-
- [1] D Weihs, “A hydrodynamical analysis of fish turning manoeuvres,” *Proceedings of the Royal Society of London B: Biological Sciences* **182**, 59–72 (1972).
 - [2] Michael Sfakiotakis, David M Lane, and J Bruce C Davies, “Review of fish swimming modes for aquatic locomotion,” *IEEE Journal of Oceanic Engineering* **24**, 237–252 (1999).

- [3] Xiaobo Tan, Michael Carpenter, John Thon, and Freddie Alequin-Ramos, “Analytical modeling and experimental studies of robotic fish turning,” in *Proceedings of the 2010 IEEE International Conference on Robotics and Automation* (IEEE, 2010) pp. 102–108.
- [4] Huosheng Hu, Jindong Liu, Ian Dukes, and George Francis, “Design of 3D swim patterns for autonomous robotic fish,” in *Proceedings of the 2006 IEEE/RSJ International Conference on Intelligent Robots and Systems* (IEEE, 2006) pp. 2406–2411.
- [5] Zongshuai Su, Junzhi Yu, Min Tan, and Jianwei Zhang, “Implementing flexible and fast turning maneuvers of a multijoint robotic fish,” *IEEE/ASME Transactions on Mechatronics* **19**, 329–338 (2014).
- [6] Junzhi Yu, Min Tan, Shuo Wang, and Erkui Chen, “Development of a biomimetic robotic fish and its control algorithm,” *IEEE Transactions on Systems, Man, and Cybernetics, Part B (Cybernetics)* **34**, 1798–1810 (2004).
- [7] Jindong Liu and Huosheng Hu, “Mimicry of sharp turning behaviours in a robotic fish,” in *Proceedings of the 2005 IEEE International Conference on Robotics and Automation* (IEEE, 2005) pp. 3318–3323.
- [8] L Cen and A Erturk, “Bio-inspired aquatic robotics by untethered piezohydroelastic actuation,” *Bioinspiration & Biomimetics* **8**, 016006 (2013).
- [9] Cornelis A Van Eysden and John E Sader, “Frequency response of cantilever beams immersed in viscous fluids with applications to the atomic force microscope: Arbitrary mode order,” *Journal of Applied Physics* **101**, 044908 (2007).
- [10] Peter Derek Yeh and Alexander Alexeev, “Free swimming of an elastic plate plunging at low reynolds number,” *Physics of Fluids* **26**, 053604 (2014).
- [11] Peter Derek Yeh and Alexander Alexeev, “Effect of aspect ratio in free-swimming plunging flexible plates,” *Computers & Fluids* **124**, 220–225 (2016).
- [12] Z Jane Wang, James M Birch, and Michael H Dickinson, “Unsteady forces and flows in low Reynolds number hovering flight: Two-dimensional computations vs robotic wing experiments,” *Journal of Experimental Biology* **207**, 449–460 (2004).
- [13] Alexander Alexeev, Rolf Verberg, and Anna C Balazs, “Modeling the motion of microcapsules on compliant polymeric surfaces,” *Macromolecules* **38**, 10244–10260 (2005).
- [14] Alexander Alexeev, Rolf Verberg, and Anna C Balazs, “Modeling the interactions between deformable capsules rolling on a compliant surface,” *Soft Matter* **2**, 499–509 (2006).

- [15] Matthew Ballard, Zachary Grant Mills, Samuel Beckworth, and Alexander Alexeev, “Enhancing nanoparticle deposition using actuated synthetic cilia,” *Microfluidics and Nanofluidics* **17**, 317–324 (2014).
- [16] Alexander Alexeev and Anna C Balazs, “Designing smart systems to selectively entrap and burst microcapsules,” *Soft Matter* **3**, 1500–1505 (2007).
- [17] Zachary Grant Mills, Basat Aziz, and Alexander Alexeev, “Beating synthetic cilia enhance heat transport in microfluidic channels,” *Soft Matter* **8**, 11508–11513 (2012).
- [18] Hassan Masoud, Benjamin I Bingham, and Alexander Alexeev, “Designing maneuverable micro-swimmers actuated by responsive gel,” *Soft Matter* **8**, 8944–8951 (2012).
- [19] Hassan Masoud and Alexander Alexeev, “Resonance of flexible flapping wings at low Reynolds number,” *Physical Review E* **81**, 056304 (2010).
- [20] Peter D Yeh and Alexander Alexeev, “Biomimetic flexible plate actuators are faster and more efficient with a passive attachment,” *Acta Mechanica Sinica* **32**, 1001–1011 (2016).
- [21] Peter Derek Yeh, Yuanda Li, and Alexander Alexeev, “Efficient swimming using flexible fins with tapered thickness,” *Physical Review Fluids* **2**, 102101 (2017).
- [22] A J C Ladd and R Verberg, “Lattice-Boltzmann simulations of particle-fluid suspensions,” *Journal of Statistical Physics* **104**, 1191–1251 (2001).
- [23] Cyrus K Aidun and Jonathan R Clausen, “Lattice-Boltzmann method for complex flows,” *Annual Review of Fluid Mechanics* **42**, 439–472 (2010).
- [24] Sauro Succi, *The lattice Boltzmann equation: For fluid dynamics and beyond* (Oxford University Press, 2001).
- [25] Gavin A Buxton, Christopher M Care, and Douglas J Cleaver, “A lattice spring model of heterogeneous materials with plasticity,” *Modelling and Simulation in Materials Science and Engineering* **9**, 485–497 (2001).
- [26] Martin Ostojca-Starzewski, “Lattice models in micromechanics,” *Applied Mechanics Reviews* **55**, 35–60 (2002).
- [27] Mhamed Bouzidi, Mouaouia Firdaouss, and Pierre Lallemand, “Momentum transfer of a Boltzmann-lattice fluid with boundaries,” *Physics of Fluids* **13**, 3452–3459 (2001).
- [28] Hudong Chen, Olga Filippova, J Hoch, K Molvig, Rick Shock, Chris Teixeira, and Raoyang Zhang, “Grid refinement in lattice Boltzmann methods based on volumetric formulation,” *Physica A: Statistical Mechanics and its Applications* **362**, 158–167 (2006).

- [29] Peter Derek Yeh, *Fast and efficient locomotion using oscillating flexible plates*, Ph.D. thesis, Georgia Institute of Technology (2016).
- [30] See Supplemental Material at [URL] for flow structures generated by the swimmer.
- [31] V Raspa, S Ramanarivo, B Thiria, and R Godoy-Diana, “Vortex-induced drag and the role of aspect ratio in undulatory swimmers,” *Physics of Fluids* **26**, 041701 (2014).